Blade Surface Pressure Measurements in the Field and Their Usage for Aerodynamic Model Validation

Fritz, Erik; Boorsma, Koen; Caboni, Marco; Herrig, Andreas

Important note
To cite this publication, please use the final published version (if applicable).
Please check the document version above.

WILEY

RESEARCH ARTICLE

Blade Surface Pressure Measurements in the Field and Their Usage for Aerodynamic Model Validation

Erik Fritz[1,2] | Koen Boorsma[1] | Marco Caboni[1] | Andreas Herrig[3]

[1]Wind Energy, TNO Energy Transition, Petten, Netherlands | [2]Faculty of Aerospace Engineering, TU Delft, Delft, Netherlands | [3]LM Wind Power, GE Renewable Energy, Garching b. München, Germany

Correspondence: Erik Fritz (e.fritz@tno.nl)

ABSTRACT

This study presents results from a long-term measurement campaign on a research wind turbine in the field. Pressure measurements are conducted at 25% blade radius over several months. Together with inflow measurements provided by a LiDAR system, they form an extensive dataset, which is used in the validation of numerical aerodynamic models. The model validation is conducted based on both ten-minute average data as well as time-resolved unsteady data. Initially, it is investigated how representative ten-minute average pressure measurements are of the underlying unsteady aerodynamics. Binned ten-minute average pressure distributions are then analysed together with their numerical counterpart, consisting of a combination of rotor and airfoil level aerodynamic/aeroelastic simulation results using average environmental and operating conditions as input. Finally, time-resolved measurements and simulation results are compared, validating the aeroelastic tools' capability to reproduce unsteady aerodynamics.

Overall, reasonable agreement is found between numerical simulations and field experiment data showcasing two aspects: Numerical tools based on blade element momentum theory and panel methods with viscous-inviscid interaction remain relevant for simulating modern multi-megawatt wind turbines, and long-term pressure measurements provide invaluable means for validating such tools.

1 | Introduction

Experiments on wind turbines play a vital role in progressing wind turbine technology. Not only do they help in improving the understanding of, for example, the turbine's aerodynamic, aeroelastic or acoustic characteristics, but the gathered data can also be used to validate and improve numerical models that aim to simulate reality as closely as possible. In this context, pressure measurements are a useful tool to gain insight into local blade aerodynamics.

Historically, the wind energy community has conducted multiple experiments on field turbines, many of which included pressure measurements. At the TNO Wind Energy (formerly ECN)

facilities, a two-bladed research turbine of 25-m diameter was operated. Pressure measurements at three radial locations were used to, among others, study the boundary layer's transition behaviour [1]. The National Renewable Energy Laboratory (NREL) conducted the Unsteady Aerodynamics Experiment (UAE) in multiple phases. Phases I–IV, executed between 1989 and 1997, were field experiments on a three-bladed rotor of 10-m diameter where both pressure distributions and blade loads were measured [2, 3]. Imperial College and Rutherford Appleton Laboratory measured pressures at six radial locations of a three-bladed turbine with 17-m diameter. Between 1989 and 1993, the Technical University of Denmark (DTU) ran several measurement campaigns on a three-bladed rotor of 19-m diameter, investigating 3D flow effects

on a rotating blade and studying its effect on airfoil characteristics [4, 5]. At the Technical University of Delft (TUD), experiments on a two-bladed rotor of 10-m diameter with pressure taps at four radial stations were conducted [6]. At Mie University, pressure distributions at midspan of a three-bladed with 10-m diameter were measured and compared alongside with the integrated forces for different yaw angles [7]. A more detailed summary of the field experiments described so far is given in the final report of IEA Annex XVIII [8]. Falling into the same range of rotor size, an Enercon E30 research turbine with 29.6-m diameter is operated on the campus of Flensburg University. Employing pressure and hot-film sensors, the airfoil boundary layer was characterised [9].

While all experiments mentioned so far undoubtedly contribute to the scientific progress in wind turbine aerodynamics, they were all conducted on turbines of smaller than current state-of-the-art size and power rating. One example of a field experiment close to modern wind turbine scales is the DAN-AERO MW project conducted by DTU in collaboration with LM Glasfiber (nowadays LM Wind Power), Siemens Wind Power (nowadays Siemens Gamesa), Vestas and DONG Energy (nowadays Ørsted) [10, 11]. Here, inflow characteristics were measured on a Siemens 3.6-MW turbine using five-hole pitot tubes and on an NM80 2-MW wind turbine using a meteorological mast. Additionally, the NM80 turbine was equipped with pressure sensors at four radial stations and microphones for high-frequency measurements at the outermost station. These field pressure measurements were compared to 2D wind tunnel experiments of corresponding airfoils [12] and 3D computational fluid dynamics (CFD) [13]. The DAN-AERO database has further been used for the validation of CFD regarding spanwise blade loading [14], rotor induction [15] and aerodynamics in sheared and yawed conditions [16] as well as for the validation of engineering correction models commonly used in blade element momentum theory (BEM) [17]. A validation benchmark comparing simulation results from a wide range of numerical tools suggested that it is still challenging to obtain a good match with field measurements [18]. Furthermore, DTU and Siemens Gamesa investigated the impact of an active trailing edge flap using measurements obtained with a pressure belt on a 4.3-MW wind turbine [19] and measurements were used to validate aeroelastic simulations [20]. Another example of large-scale field experiments is the ongoing RAAW experiment conducted on a 2.8-MW research wind turbine by GE Vernova, NREL and Sandia National Laboratories [21]. This experiment aims to provide an exhaustive validation dataset by measuring the flow field upstream and downstream of the turbine [22] and the turbine's loads and performance. The measurements have been used to inform wind field reconstruction methods based on large-eddy simulations [23] and to validate load and performance predictions by aeroservoelastic simulations [24]. It should be noted, that research conducted on state-of-the-art wind turbines is often done in collaboration with industrial partners. As a consequence, results can only partly be disseminated to protect commercial interests.

While the focus of this paper is on field experiments, two wind tunnel experiments, namely UAE Phase VI and the MEXICO campaigns, significantly contributed to the validation of aerodynamic models, partially due to their pressure measurements. For UAE Phase VI, conducted in 2000, a two-bladed rotor of 10-m diameter was heavily instrumented and placed in the NASA Ames wind tunnel [25]. The MEXICO experiment was conducted in 2006 in the German Dutch Wind Tunnel (DNW). Detailed aerodynamic measurements including pressure, loads and 3D flow field characteristics using Particle Image Velocimetry (PIV) were taken on a three-bladed rotor with 4.5-m diameter [26]. Its successor project 'New Mexico' was conducted in 2014 to obtain additional data [27]. Results of these two experimental campaigns have been analysed in great detail and have been used for the validation/calibration of simulation tools of varying fidelity. For an extensive review of the literature related to these two experiments, the reader is referred to the work of Schepers and Schreck [28].

One central development in the field of wind turbine technology is the ever-growing size of the rotor. Modern wind turbine blades surpass lengths of 100 m and are becoming increasingly slender and flexible structures. The scalability of previously obtained research results has to be questioned, leading to two important challenges: First, field research needs to be conducted to understand the aerodynamic and aeroelastic behaviour of these larger wind turbines. Second, in contrast to the turbines themself, the numerical tools used to design them remain largely unchanged. It is thus of utmost importance to continuously validate the simulation algorithms' capability to accurately predict the aerodynamic and aeroelastic behaviour of wind turbines. As discussed above, few extensive measurement campaigns that capture a vast range of operating and environmental conditions are available for such validation exercises.

In the present research effort, a long-term measurement campaign is conducted on a 3.8-MW research wind turbine with a rotor diameter of 130 m. Complimenting recent available literature, this research wind turbine size enables the acquisition of data more representative of state-of-the-art wind turbines. Pressure measurements are performed at 25% of the blade radius, where the blade is defined by a 38% thick airfoil, and a ground-based LiDAR system provides inflow measurements. Limited experimental data exists for airfoils of comparable thickness, particularly not in rotating conditions in the field. Measurements are logged over several months, resulting in an extensive field experiment database. In this study, the pressure measurements are used to validate aerodynamic models on the physical scale of rotor and airfoil and on the time scale of ten-minute averages and fully time-resolved data.

This research paper is built up as follows: Section 2 presents the measurement setup and the data reduction approach. Furthermore, the numerical simulation models employed in this study, as well as the methodology of estimating the angle of attack from the pressure measurements, are introduced. Section 3 presents results from analysing the experimental data based on long-term ten-minute average measurements as well as time-resolved unsteady measurements. Finally, conclusions are drawn in Section 4.

2 | Methodology

2.1 | Measurement Set-Up

2.1.1 | Test Site

A long-term validation campaign is performed on a 130-m diameter, three-bladed 3.8-MW wind turbine featuring variable speed and active blade pitch (to vane) control at 110-m hub height. As

of spring 2021, this turbine has become operational at the test site of ECN Wind Energy Facilities (EWEF) in Wieringerwerf, the Netherlands [29, 30]. An overview of the test site is given in Figure 1.

The test site and its surroundings are characterised as flat terrain, consisting of mainly agricultural areas, with single farmhouses and rows of trees. The EWEF farm is very well suited for an investigation into effects at full scale because of its state-of-the-art turbines and the comprehensive and reliable measurement infrastructure for turbine and meteorological data. The TIADE turbine is located at the most westerly spot within a row of prototypes that are positioned on a line that is roughly oriented West to East, hence resulting in a relatively large undisturbed sector which includes the prevailing southwesterly wind direction.

The turbine has been instrumented in accordance with IEC measurement campaigns for power and loads. Wind speed measurements have been taken from a ground-based LiDAR located 280 m in southwesterly direction, which measures at 11 different heights from 42 to 188 m. Also, air pressure and temperature are measured at a nearby meteorological mast. In addition to the ground-based LiDAR, two forward-looking nacelle-based LiDARs are operational on the turbine, plus a scanning LiDAR positioned 912 m in southwesterly direction to measure wake characteristics.

2.1.2 | Pressure Measurements

At 25% of the blade radius, 31 pressure taps are used to measure the pressure distribution around the blade cross-section. The pressure taps on the blade surface are connected to two Scanivalve DSA3218-PTP pressure scanners through pressure tubes. Each pressure scanner can accommodate 16 signals and typically has a 0.05% full-scale long-term accuracy. The reference pressure, measured in the turbine hub, is connected to the pressure scanners by a tube of approximately 15 m length.

At the measurement location, the blade geometry is defined by a 38% thick airfoil closely resembling the DU-00-W-401 airfoil. Its geometry is a blend between the DU-00-W-401 airfoil and a proprietary airfoil by LM Wind Power, which is why limited information regarding its characteristics can be made publicly available. The pressure sensor layout is designed using a genetic algorithm optimisation routine [32] to represent the pressure distribution as accurately as possible throughout the operational range of the turbine. A schematic of the measurement system, the optimised sensor layout and the inflow conditions are shown in Figure 2.

Spanwise sensor staggering is applied to avoid any turbulence created by the upstream sensors interfering with measurements of the sensors further downstream. On top of that, the streamlines on the blade surface at 25% radius will be curved due to the circular motion of the blade. Therefore, an additional arc is added to the spanwise staggered sensor positions. The resulting differences in the individual sensors' spanwise location entail a negligible change in the local airfoil shape.

2.2 | Data Reduction

2.2.1 | Correction for Centrifugal Forces

For each tap, the pressure is measured as the differential pressure Δp between the blade surface pressure and a reference pressure. To derive the blade surface pressure, Bernoulli's equation is employed, which in differential form reads

$$\frac{\mathrm{d}p}{\rho} + V\mathrm{d}V + g\,\mathrm{d}z = 0 \tag{1}$$

where p is the static pressure, ρ is the density of air, V is a velocity, g is the gravitational constant and z is the height. The height of a blade cross-section can be expressed as

$$z(r, \theta) = z_{hub} + r(\cos\zeta\cos\tau\cos\theta - \sin\zeta\sin\tau) \tag{2}$$
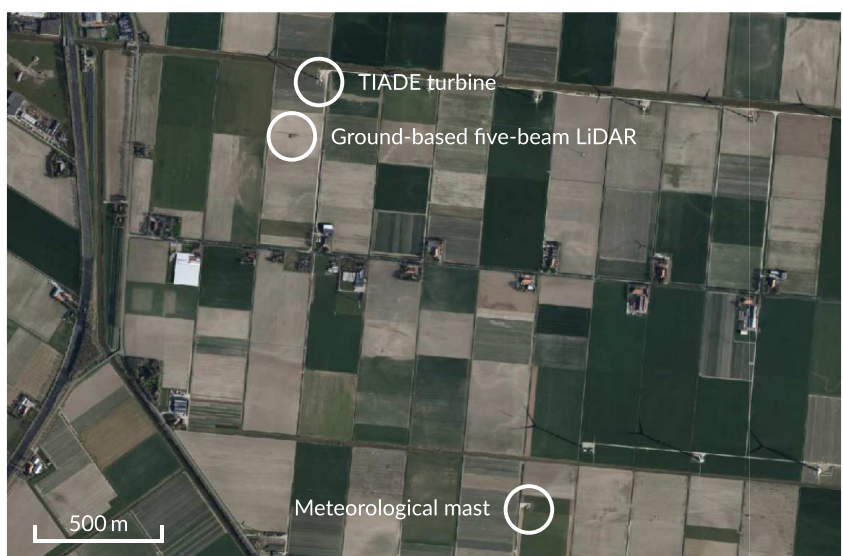
FIGURE 1 | Overview of the test site, map derived from data provided by PDOK (Publieke Dienstverlening op de Kaart), licensed under the CC-BY-4.0 license [31].
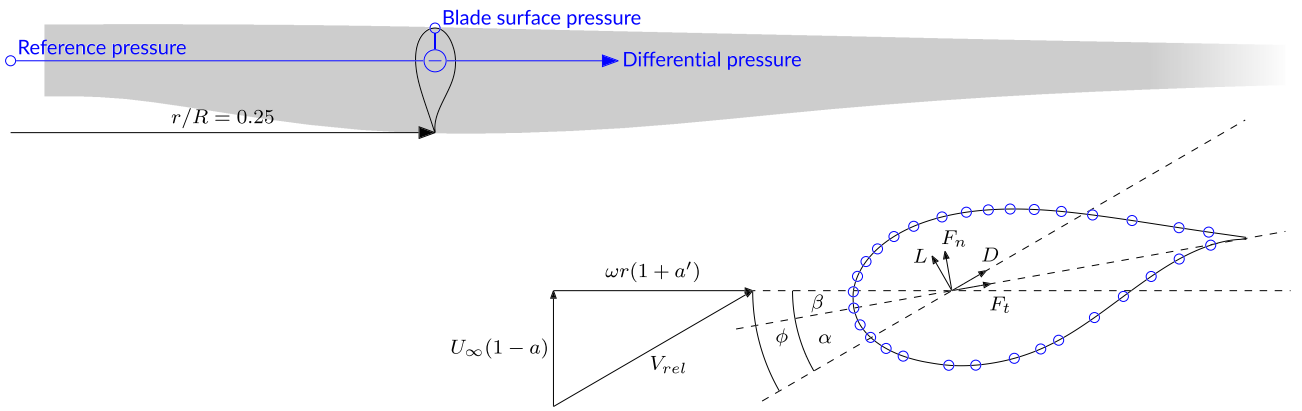
FIGURE 2 | Schematic of the measurement setup and DU-00-W-401 airfoil with pressure taps and inflow conditions.

where z_{hub} is the hub height, r is the radial position, ζ is the cone angle, τ is the tilt angle and θ is the azimuthal angle ($\theta = 0$ refers to the vertical upward blade position). Here, straight blades without prebend, sweep or deformation are assumed. Applying partial derivatives with respect to the variable quantities r and θ, dz becomes

$$dz = \frac{\partial z}{\partial r}\, dr + \frac{\partial z}{\partial \theta}\, d\theta \tag{3}$$

where

$$\frac{\partial z}{\partial r} = \cos\zeta \cos\tau \cos\theta - \sin\zeta \sin\tau \tag{4}$$

and

$$\frac{\partial z}{\partial \theta} = -r \cos\zeta \cos\tau \sin\theta \tag{5}$$

Substituting Equations (3)–(5) into Equation (1), Bernoulli's equation now reads

$$\frac{dp}{\rho} + V\,dV + g(\cos\zeta \cos\tau \cos\theta - \sin\zeta \sin\tau)\,dr \\ - g\,r \cos\zeta \cos\tau \sin\theta\, d\theta = 0 \tag{6}$$

Assuming two points with p_1, V_1, r_1, θ_1 and p_2, V_2, r_2, θ_2, Bernoulli's equation yields

$$\frac{p_2 - p_1}{\rho} + \frac{V_2^2 - V_1^2}{2} + g(\cos\zeta \cos\tau \cos\theta - \sin\zeta \sin\tau)\,(r_2 - r_1) \\ + g\,r \cos\zeta \cos\tau\,(\cos\theta_2 - \cos\theta_1) = 0 \tag{7}$$

Assuming further that $p_1 = p_\infty$, $V_1 = U_\infty$, $r_1 = 0$, $p_2 = p_{surf}$, $V_2 = V$, $r_2 = r_{PS}$ and $\theta_1 = \theta_2$, then the pressure on the blade surface p_{surf} can be expressed as

$$p_{surf} = p_\infty + \frac{\rho}{2}\left(U_\infty - V\right)^2 - \rho g r_{PS}(\cos\zeta \cos\tau \cos\theta - \sin\zeta \sin\tau) \tag{8}$$

Here, p_∞ and U_∞ are the freestream static pressure and velocity, respectively, at hub height, V is the velocity over the airfoil and r_{PS} is the radial position of the pressure sensors.

Bernoulli's equation is employed again to derive the pressure on the reference side of the pressure sensor. The air in the reference tube experiences an additional radial acceleration field so that

$$\frac{dp}{\rho} + V\,dV + g\,dz + \omega^2 r\,dr = 0 \tag{9}$$

where ω is the angular velocity of the turbine. Similar to the blade surface side, this leads to

$$\frac{p_2 - p_1}{\rho} + \frac{V_2^2 - V_1^2}{2} + g(\cos\zeta \cos\tau \cos\theta - \sin\zeta \sin\tau)\,(r_2 - r_1) \\ + g\,r \cos\zeta \cos\tau\,(\cos\theta_2 - \cos\theta_1) + \frac{\omega^2}{2}\,(r_2^2 - r_1^2) = 0 \tag{10}$$

Assuming $p_1 = p_{hub}$, $V_1 = 0$, $r_1 = 0$, $p_2 = p_{ref}$, $V_2 = 0$, $r_2 = r_{PS}$ and $\theta_1 = \theta_2$, then the pressure on the sensor's reference side p_{ref} can be expressed as

$$p_{ref} = p_{hub} - \rho g r_{PS}(\cos\zeta \cos\tau \cos\theta - \sin\zeta \sin\tau) - \frac{\rho}{2}\omega^2 r_{PS}^2 \tag{11}$$

where p_{hub} is the static pressure in the hub. The measured difference between blade surface pressure p_{surf} and reference pressure p_{ref} is then

$$\Delta p = p_\infty + \frac{\rho}{2}\left(U_\infty - V\right)^2 - p_{hub} + \frac{\rho}{2}\omega^2 r_{PS}^2 \tag{12}$$

As can be seen from Equation (12), the hydrostatic pressure changes experienced on the blade surface are equal to those on the reference side of the pressure sensors and thus cancel each other out. In contrast to that, the measured data has to be corrected for centrifugal effects. The ratio of the centrifugal pressure to the dynamic pressure $p_{dyn} = \frac{\rho}{2} V_{rel}^2$ is

$$\frac{\Delta p_{cent}}{p_{dyn}} = \frac{\frac{\rho}{2}\omega^2 r_{PS}^2}{\frac{\rho}{2}V_{rel}^2} \tag{13}$$

The relative velocity can be expressed as $V_{rel} = \omega r \sqrt{\frac{1}{\lambda^2}\frac{R^2}{r^2}(1-a)^2 + (1+a')^2}$. With $r/R = 0.25$, assuming axial and tangential induction factors of $a = 0.3$ and $a' = 0$, respectively, and a tip-speed ratio of $\lambda = 9$, then $\frac{\Delta p_{cent}}{p_{dyn}} = 0.91$, showcasing the importance of the correction for centrifugal loads. To eliminate centrifugal effects from the measurements, the measured differential pressure is corrected so that

$$\Delta p_{cor} = \Delta p - \frac{\rho}{2}\omega^2 r_{PS}^2 \tag{14}$$

2.2.2 | Estimation of the Local Inflow Velocity

The wind profile is provided by a ground-based LiDAR system. Mathematically, the wind profile including shear can be described by a power law curve

$$V_{hor}(z) = V_{hor}(z_{ref})\left(\frac{z}{z_{ref}}\right)^{n_s} \tag{15}$$

where V_{hor} is the horizontal wind velocity, z_{ref} is a reference height often taken to be the hub height and n_s is the shear exponent. The shape of the wind profile is time-dependent, thus inducing time-dependent loads on the turbine. To estimate the change of loading with time, a good approximation of the instantaneous wind profile is desirable. For time-resolved analyses, a shear exponent $n_s(t)$ is fit to the instantaneous wind profile for each time stamp and the time-varying wind profile is calculated as $V_{hor}(z, t) = V_{hor}(z_{hub}, t)\left(\frac{z(t)}{z_{hub}}\right)^{n_s(t)}$. This approach enables the estimation of the horizontal wind speed $V_{hor,est}$ at a given time and height. As such, it can be used to estimate the inflow conditions at the blade location where the pressure sensors are located. The velocity components normal and tangential to the rotor plane/cone are given by

$$V_n = V_{hor}\cos\psi\cos\tau \tag{16}$$

$$V_t = \omega r\cos\zeta + V_{hor}(\sin\tau\sin\theta - \sin\psi\cos\theta) \tag{17}$$

where ψ is the yaw misalignment angle. Neglecting axial and tangential induction, the relative velocity at the blade is

$$V_{rel} = \sqrt{V_n^2 + V_t^2} \tag{18}$$

2.2.3 | Processing of Ten-Minute Statistics

The power, loads, pressures and turbine operational measurement signals of the research turbine, together with the wind speed measurements of the ground-based LiDAR and atmospheric measurements of the meteorological mast, have been used for this analysis. Ten-minute statistics in the form of mean
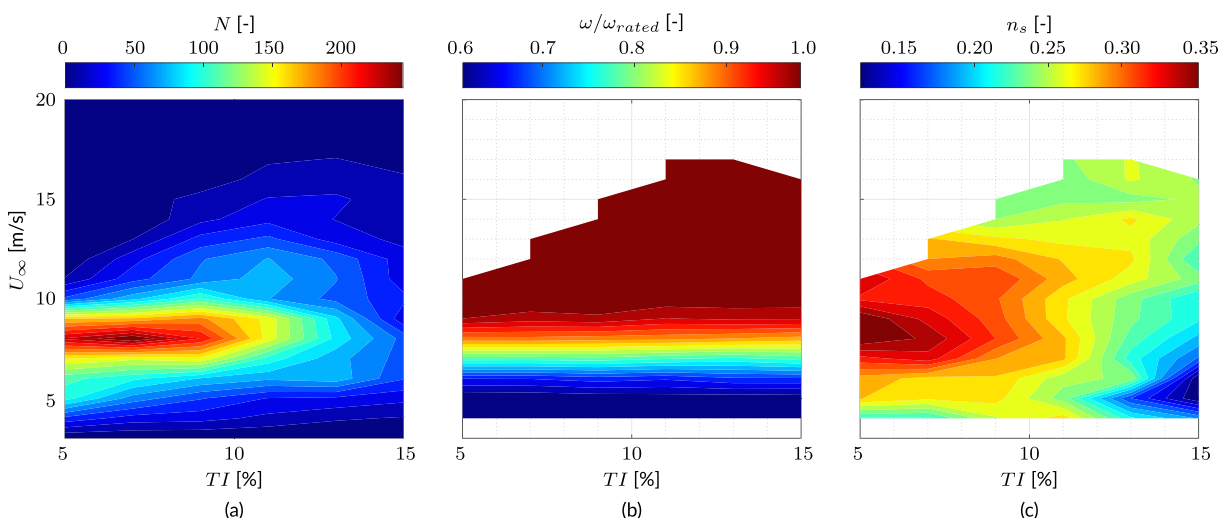
$\overline{\xi}_{10}$, standard deviation $\sigma_{10}(\xi)$, minimum $\xi_{10,min}$ and maximum $\xi_{10,max}$ have been retrieved from the database, resulting in a large number of ten-minute samples. Here, the arbitrary variable ξ represents the measurement signals. After retrieving the statistics from the database, a second data reduction step is performed to filter out erroneous samples, outliers, and complex inflow instances that are too hard to replicate with aeroelastic simulations. The underlying ten-minute samples are excluded from the dataset for selected signals

- when a measurement signal is not recorded, for example, due to a malfunction, resulting in a non-numeric value (NaN),

- when the wind direction falls outside the undisturbed wind sector, leading to wake effects from neighbouring turbines,

- when the turbine is not in normal operation conditions in power production, discarding parked and idling cases, or

- when large yaw misalignment, extreme turbulence and shear occur.

Starting with about 48,000 ten-minute samples from the database for a 9-month period featuring a constant blade configuration, about 4000 samples remained after application of the above-specified filtering. These ten-minute samples and their statistics are used for the analyses presented in Sections 3.1 and 3.2. The distribution of these samples as a function of wind speed and turbulence intensity TI is illustrated in Figure 3a.

Aerodynamic forces and pressures are influenced by atmospheric conditions linearly through the air density. The variation of the air density can be shown to lie between 1.2 and 1.3 kg/m^3 for the selected samples. To account for these changes, the measured aerodynamic pressures are corrected to a reference air density of 1.225 kg/m^3 using the ideal gas law.

To characterise trends in the data, the ten-minute samples are binned. Bin averaging is applied to the resulting data set both in wind speed and turbulence intensity. The standard error of the mean within each bin is calculated using


FIGURE 3 | Distribution of number of ten-minute samples (a), non-dimensionalised rotor speed (b) and vertical wind shear exponent (c) as function of binned wind speed and TI for the current data set.

$$S(\overline{\xi}) = \frac{\sigma_{bin}(\overline{\xi})}{\sqrt{N}} \qquad (19)$$

where $\sigma_{bin}(\overline{\xi})$ is the standard deviation of the bin data samples and N is the number of samples per bin. This standard error is a measure of the ten-minute mean's repeatability over the various samples within one bin. Additionally, the mean value of the ten-minute standard deviations of the samples in one bin $\overline{\sigma}_{10}(\xi)$ is a measure of the variability of the regarded signal in a particular bin. A minimum of six samples is chosen as requirement for a bin to have a valid average value. The measured data is binned for inflow velocities between 3 and 20 m/s with an increment of 1 m/s and for turbulence intensity values between 5% and 15% with an increment of 2%.

Figure 3b shows the binned rotor speed non-dimensionalised by the rated rotor speed. It can be observed, that the rotor speed is a function of the wind speed rather than of the turbulence intensity. Combining the data from Figure 3a,b, it becomes clear that the majority of the available data is located close to where the rated rotor speed is reached.

Unsteady loads are highly influenced by turbulence and its intensity as well as other wind non-uniformities such as vertical shear. If bin-averaged load results are compared, it is important to also consider these to prevent bias. It is known that *TI* and vertical wind shear are correlated, in the sense that nighttime features high shear and low *TI*, while daytime features higher *TI* and lower shear. This relationship is once more illustrated in Figure 3c for the current dataset. It is acknowledged that this relationship makes it difficult to distinguish between the effects of shear and turbulence intensity in the bin-averaged dataset.

2.2.4 | Processing for the Time-Resolved Analysis

In the second step of the analysis presented here, measurements and simulations are compared on a time-resolved basis. The pressure measurements are sampled at a frequency of 256 Hz. Considering multiple months of measurements, the amount of data rapidly outgrows sizes manageable in standard data processing software. Thus, several steps are taken in addition to the filtering for time period, rotational speed, turbine state, wind direction and invalid data described in the previous section:

1. On and after rainy days, water accumulates in the pressure tubes, which expresses itself in 'spiky' pressure measurements, where sensors containing water in their connecting tube exhibit a different mean pressure level due to the density of water. Either centrifugal forces drive the water out of the tubes again or the tubes can be purged to return to undisturbed data acquisition. While this can average out to an extent in the ten-minute average values, it is clearly visible in the time-resolved data. Thus, a filter for the smoothness of the pressure distribution is applied. Any ten-minute time series containing too many time stamps that fail that filter is discarded. This filter leads to a strong cut in available data but ensures that only measurement periods with very clean data are used.

2. The data undisturbed by rain are downsampled to a frequency of 8 Hz to make the amount of data more manageable. At rated rotor speed, this sampling increment corresponds to about ten-degree rotor rotation, which is deemed sufficient to capture most unsteady effects.

3. Even during ten minutes, the environmental and operating conditions can vary significantly, making a comparison to simulations on a time-resolved level difficult. Therefore, the ten-minute time series are further broken down into two-minute intervals. The average environmental (ρ, U_∞, n_s) and operating (ω, β, ψ) conditions are then used as input to steady aeroelastic simulations.

After this filtering, approximately 1300 two-minute time series remain, which will be compared against an equal number of aeroelastic simulations. This comparison is presented in Section 3.3.

2.3 | Numerical Tools

In the present study, multiple simulation tools are employed. Rotor-level aerodynamics are solved using tools based on blade element momentum theory. Phatas is a time-domain aeroelastic simulation software currently developed and maintained by LM Wind Power [33] (with last publicly available documentation by Lindenburg [34]). It solves the dynamic response of wind turbines by coupling the aerodynamic loads calculated by a BEM algorithm with a non-linear structural solver. To make use of more advanced aerodynamic models, the TNO-inhouse aerodynamic simulation suite AeroModule [35] is coupled to the structural solver of Phatas. This coupled tool is referred to as Phataero. Unsteady aerodynamic effects are accounted for by the first-order model by Snel [36] and Prandtl root and tip corrections are active.

Airfoil-level aerodynamics are solved using the 2D panel code RFOIL which couples the potential flow solution of an airfoil to a boundary layer solver [37]. The tool is based on the widely known XFOIL code developed by Drela [38], but tailored specifically to the simulation of rotating airfoils as used among others on wind turbines. Previous research has shown RFOIL to be a valid tool for the analysis of airfoils with a relative thickness comparable to the one under investigation here [39].

2.4 | Estimation of the Angle of Attack

Based on the pressure measurement setup described in Section 2.1.2, local aerodynamic quantities can be measured directly or estimated from the measurements. The local chord normal force F_n and chord tangential force F_t can be derived by integrating the measured pressure distribution p along the surface of the blade cross-section S_B

$$\begin{bmatrix} F_t \\ F_n \end{bmatrix} = \oint_{S_B} \overline{n}\, p\, ds \qquad (20)$$

where $\overline{n}$ is the surface normal vector.

Another aerodynamic quantity of interest is the angle of attack. The determination of the angle of attack in rotating systems is a recognised challenge; it is a subquestion of IEA Task 47, which aims at scientific cooperation in the field of detailed aerodynamic measurements on MW-scale wind turbines. Multiple methods for estimating the angle of attack on rotating wind turbine blade sections have been applied in the past.

When detailed information on the flow around an investigated blade cross-section is available, for example, in the form of particle image velocimetry data or numerical simulation results, the angle of attack can be estimated by calculating the axial induction, either as annulus average axial induction [40, 41], as the induced axial velocity at the blade location [42] or as the wake induction at the plane exactly between two blades [43]. Other approaches use the velocity field in the vicinity of the blade to estimate the bound circulation strength, which, in turn, can be used to estimate local induced velocity and consequently the angle of attack [44–46]. Furthermore, these two approaches can be combined, initially calculating the vorticity distributed over the blade surface and then calculating the axial induction based on the velocity field around the blade from which the induction of the bound vortex has been subtracted [47]. Several of the methods described here were applied to computational fluid dynamics (CFD) simulations of a 10-MW reference wind turbine in axial flow by Rahimi et al. [48] and of the MEXICO rotor in yawed inflow by Vimalakanthan et al. [49].

In many experimental setups, the available data is limited to pressure distributions and the resulting sectional forces. The above-mentioned methodologies are, therefore, often not suitable to determine the angle of attack based on experimental data [50]. For such cases, several other methods have been developed.

The **inverse BEM method**, developed by Bruining et al. [51] and Snel et al. [52], uses measured sectional forces and inflow velocities to determine the axial and tangential induction factors based on blade element momentum theory. Once the induction is known, the inflow angle and, consequently, the angle of attack can be calculated. Laino et al. [53] and Bak et al. [54] used the inverse BEM method to derive the angle of attack and 3D airfoil characteristics using the measurements of the UAE Phase VI experiment. Potentier et al. developed an unsteady inverse BEM method and applied it to the field measurements of the DAN-AERO MW project [17].

When aerodynamic forces are measured at multiple radial stations, an **inverse vortex wake method** can be applied. Tangler used this approach with prescribed wake to determine the 3D airfoil characteristics based on the UAE Phase VI measurements [55, 56]. This analysis was extended by Sant et al. using a lifting line algorithm with a free wake formulation [57, 58] and Micallef et al. applied the inverse free wake approach to data from the MEXICO experiment [59].

Alternatively to these 'inverse' approaches, the angle of attack can be estimated by applying **pattern-matching**, that is, by finding the minimum deviation between the measured pressure distribution and known combinations of pressure distribution and angle of attack. These known pressure distributions can be obtained from wind tunnel measurements [12, 60, 61] or using numerical simulations [50, 62].

In the present work, a pattern-matching algorithm is chosen to estimate the angle of attack. To this end, the measured pressure distributions are compared to RFOIL simulation results. Within the estimated range of operational angles of attack, pressure distributions are simulated with an increment of $\Delta\alpha = 0.1°$. It should be noted, that these simulation results are given as non-dimensionalised pressures, whereas the measured pressures are absolute pressure values. Since the given measurement setup does not allow for an accurate estimation of both axial and tangential induction, the relative inflow velocity at the measurement blade section cannot be derived, and consequently, the pressure measurements cannot be non-dimensionalised. To make simulated and measured values comparable, the pressure distributions are scaled to an arbitrary scale (here, zero to one is used), and the pattern matching hence becomes a matching of the shapes of pressure distributions.

The pattern-matching algorithm's accuracy could potentially be increased by allowing scaling and shifting of the measured pressure distribution instead of using a fixed arbitrary scale. These additional degrees of freedom would make a brute force approach, as used in the current implementation, computationally extremely expensive, because the angle of attack is determined on a time-resolved basis for a large number of time series. An actual optimisation scheme might then be better suited to find the closest match. The development of such an algorithm is considered outside the scope of this publication.

3 | Results and Discussion

The results presented in this section were obtained in a research project in collaboration with GE Renewable Energy and LM Wind Power. To respect their intellectual property, the tick values on most axes are omitted, and arrows indicating ranges of the presented values are shown instead.

3.1 | How Representative is a Ten-Minute Average Pressure Distribution?

In later parts of the presented study, ten-minute statistics are used as input for numerical simulations. These numerical simulations yield aerodynamic characteristics along the blade span. One of these characteristics is the local angle of attack. The angle of attack can, in turn, be used as input for RFOIL calculations that result in pressure distributions which can be compared against the measured data. By using measured data both as input to the numeric simulations and as comparison to the simulation output, the combined workflow of numerical simulations on a turbine and airfoil level can be validated. This validation procedure, however, relies on the assumption that a ten-minute average pressure distribution is representative of the mean operating conditions of the same period.

To test this assumption the following approach is chosen. For each time step, the time-resolved pressure distribution is used to estimate the time-resolved angle of attack $\alpha_{est,TS}$ according

to the approach described in Section 2.4. Averaging these time-resolved values, one mean angle of attack of the time-resolved data $\bar{\alpha}_{est,TS}$ is calculated per ten-minute time series. Additionally, the ten-minute average pressure distribution is used to estimate the angle of attack $\bar{\alpha}_{est,10}$. The correlation of these two angle of attack estimates is shown in Figure 4a coloured based on the mean measured inflow velocity. A linear correlation exists for lower angles of attack, corresponding to wind speeds up to approximately 15 m/s. For higher wind speeds and, consequently, higher angles of attack, non-linear aerodynamic phenomena, such as flow separation, occur more frequently. This leads to the ten-minute average angle of attack $\bar{\alpha}_{est,10}$ overestimating the mean time-resolved angle of attack $\bar{\alpha}_{est,TS}$. This indicates that ten-minute averaged pressure data is likely less representative of the underlying time-resolved data when obtained at higher wind speeds and should, thus, be interpreted with additional care.

Contrary to the estimated angle of attack, the mean time-resolved blade forces and the ten-minute average blade forces are identical. Using the estimated angle of attack, the chord normal and tangential forces resulting from the integrated pressure distribution can be decomposed into the estimated lift force

$$L_{est} = F_n\cos(\alpha_{est}) - F_t\sin(\alpha_{est}) \tag{21}$$

and an estimate of the lift coefficient can be obtained

$$c_{l,est} = \frac{L_{est}}{\frac{\rho}{2}V_{rel}^2 c} \tag{22}$$

where c is the local chord length.

The lift coefficient curves based on the ten-minute average angle of attack estimate and based on the average time-resolved angle of attack estimate are shown in Figure 4b,c, respectively. For comparison, the DU-00-W-401 airfoil polars obtained in a wind tunnel for a chord Reynolds number of $Re = 3 \cdot 10^6$ and clean conditions are shown. It should be noted that, on average, the chord Reynolds number in the field is approximately twice as high. Since the measurement location is close to the root, the flow is expected to be three-dimensional. Next to the two-dimensional wind tunnel polars, two lift curves corrected for three-dimensional flow effects are shown. Both corrected

lift polars are derived from the wind tunnel lift coefficient $c_{l,2D}$ using the correction model by Snel et al. [52]:

$$c_{l,3D} = c_{l,2D} + 3.1\left(\frac{c}{r}\right)^2 \left(c_{l,inv} - c_{l,2D}\right) \tag{23}$$

where $c/r = 0.2454$ and $c_{l,inv}$ is the inviscid lift coefficient. It was recommended by Montgomerie et al. to use an inviscid simulation tool such as RFOIL to generate these polars [63]. However, many BEM-based tools, including Phataero, are built to only receive viscous polars as input. In Phataero's case, the inviscid lift polar is approximated by linearly extrapolating the linear region of the viscous lift curve such that

$$c_{l,inv} = \frac{c_l\left(\alpha_{lin,max}\right) - c_l\left(\alpha_{lin,min}\right)}{\alpha_{lin,max} - \alpha_{lin,min}}\left(\alpha - \alpha_0\right) \tag{24}$$

where $\alpha_{lin,min}$ and $\alpha_{lin,max}$ define the start and end point of the lift polar's linear region, respectively, and α_0 is the angle of attack resulting in zero lift. The results of both approaches are given in Figure 4b,c.

It should be noted that the lift force measured in the field is non-dimensionalised by a velocity not accounting for induction values since these cannot accurately be determined. Therefore, the field-measured lift curves should be interpreted in terms of trends rather than absolute values when comparing them to wind tunnel data. Pre-stall, the trend of the field data matches well with that of the wind tunnel lift polar, particularly the 3D-corrected polar using inviscid polars based on RFOIL. In the field, stall occurs approximately 2° of angle of attack earlier than in the wind tunnel. Post-stall, the field data undershoots the 3D-corrected wind tunnel data and aligns better with the trend of the uncorrected 2D wind tunnel lift polar.

3.2 | Model Validation Based on Long-Term Ten-Minute Averaged Experimental Data

After the data reduction using ten-minute statistics as described in Section 2.2, trends in pressure distribution for normal operating conditions can be obtained as a function of
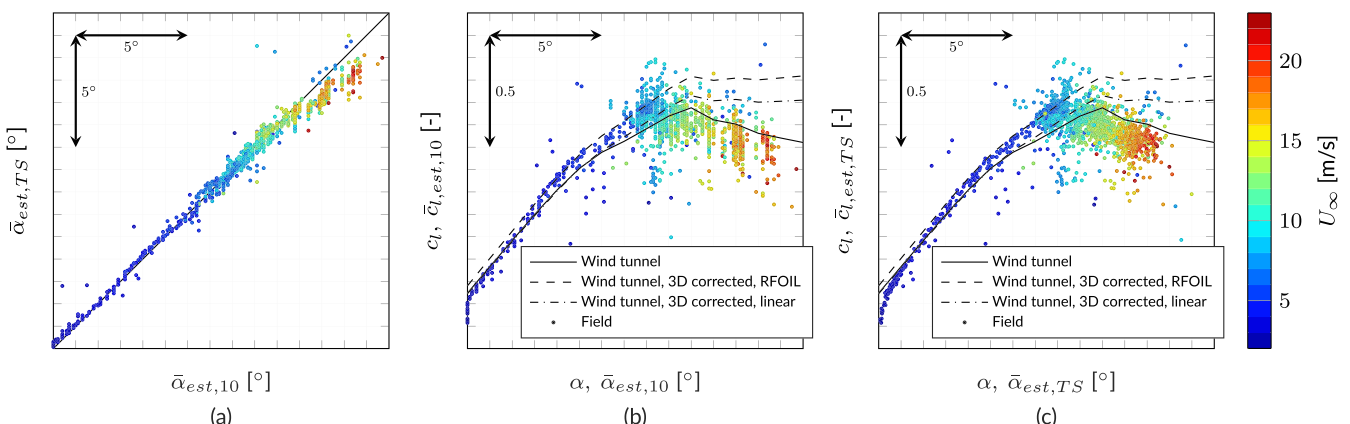

FIGURE 4 | Comparison of angle of attack estimates based on ten-minute average and time-resolved pressure distributions (a), resulting estimates of the lift coefficient vs angle of attack curves based on ten-minute average data (b) and time-resolved data (c), α and c_l refer to the values of the wind tunnel experiments while α_{est} and $c_{l,est}$ refer to the values estimated based on the field pressure data.

wind speed and turbulence intensity. Figure 5a displays for an identical mean inflow speed the effect of a larger turbulence intensity, which clearly increases the unsteadiness as illustrated by the larger uncertainty band in the plot. Besides the varying inflow conditions, it is acknowledged that these lead to larger rotor speed variations, which affect the measured pressure distribution as well. Also note the standard error, resulting from the bin average process, is indicated in the plots, demonstrating satisfactory repeatability. Figure 5b illustrates the effect of a varying wind speed, clearly changing dynamic pressure levels but also the shape of the pressure distribution indicating a difference in local angle of attack. It is noteworthy that for some measurements, for example, the suction side sensor at $x/c = 0.18$ for $U_\infty = 10\,\text{m/s}$ and $TI = 5$ %, an elevated standard error can be observed compared to neighbouring sensors while the standard deviation does not show this behaviour. It can be hypothesised that this is due to a ten-minute sample with a clogged sensor (e.g., by rainwater). This would have an influence on the mean measured pressure level, and thus the standard error of that bin, while affecting the dynamic pressure variation less.

Integration of the pressure distribution with respect to chord and thickness yields chord normal and tangential sectional forces,
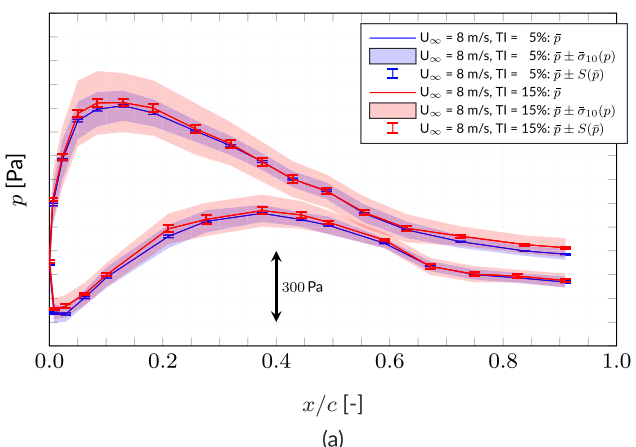
respectively, at the designated radial position. Figure 6 then illustrates the resulting chord normal and tangential force coefficient variation with wind speed, compared to Phataero simulations with both clean and rough wind tunnel measured airfoil polars used as input. Here, it is noted that the airfoil data is corrected for rotational augmentation in situ using the method of Snel [52] as explained in Section 3.1. The bin-averaged measurement values of pitch angle and rotational speed have been utilised as input for the operational conditions of the simulations. To ensure comparability, both measured and simulated forces are non-dimensionalised under neglection of induced velocities.

For the normal force variation, a good agreement in absolute level and trend is observed, provided the clean airfoil polar dataset is used. It is evident that for small wind speeds, the 3D correction of the polars ensures a slightly better match between measurements and simulation, while for wind speeds above $U_\infty = 9\,\text{m/s}$, the use of uncorrected polars yields better agreement. This observation aligns with findings from Section 3.1, where the 3D-corrected wind tunnel lift polar exceeds the field measurements for higher wind speeds.

The measured and simulated tangential force coefficients show even better agreement, again under the condition that
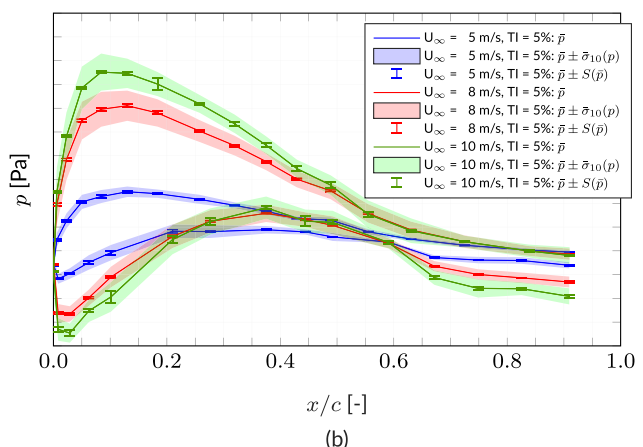
FIGURE 5 | Mean pressure distributions, 95% confidence interval and standard error, subfigure (a) showing results for $U_\infty = 10\,\text{m/s}$ with varying TI, subfigure (b) showing results for $TI = 5\%$ and varying U_∞; subfigures with identical ordinates.
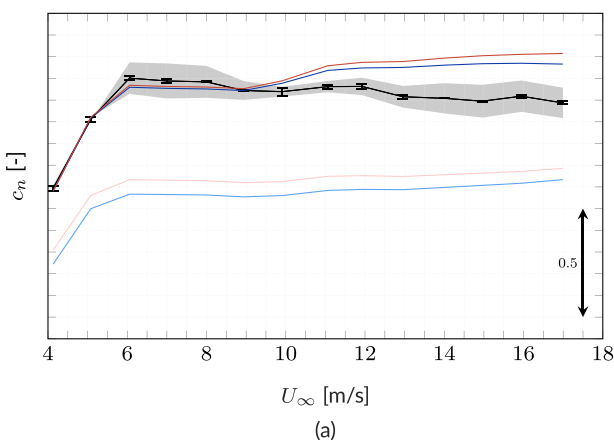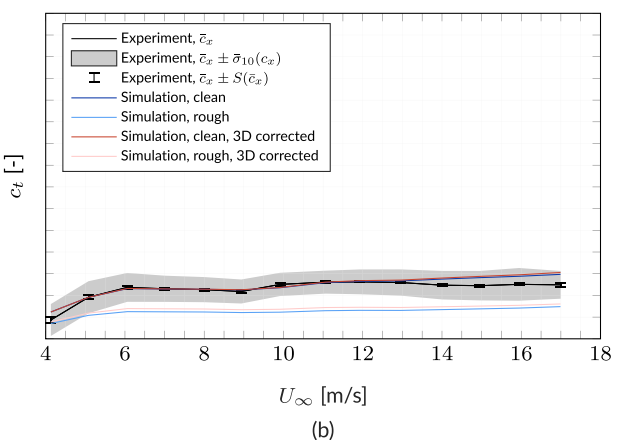

FIGURE 6 | Chord normal (a) and tangential (b) force coefficient based on measured pressure distributions and numerical simulations, legend entry c_x represents c_n and c_t in their respective subfigures; subfigures with identical ordinates.

clean polars are input to the simulation. Detectable deviations occur above $U_\infty = 13$ m/s, where the simulations predict higher tangential loading than was measured. As expected, the 3D correction has a negligible effect on the simulated tangential force coefficient. The good match between simulation and experiment is somewhat surprising given that the experimentally determined tangential force is lacking a non-negligible contribution of viscous forces. It was checked that the finite number of available pressure sensors causes a negligible error with which the inviscid tangential force coefficient is determined. Thus, it is expected that a comparison of tangential forces accounting for viscosity would result in less congruence.

The Phataero simulation results can further be used to provide RFOIL simulations with input, that is, angle of attack and chord Reynolds number. Additionally, RFOIL requires an estimate of the critical amplification factor N_{crit}, a parameter related to the boundary layer transition behaviour. The N_{crit} value is determined using a modified version of Mack's model [64], which relates N_{crit} to the local turbulence intensity. Several modifications to Mack's model exist, which improve the N_{crit} prediction for higher *TI* values [65, 66]. Here, the modification by Drela and Youngren [65] is applied, which ensures positive N_{crit} values even at high turbulence intensity values as are present in this field campaign.

The combination of Phataero and RFOIL enables a model validation on the airfoil level by comparing the simulated pressure distributions against those measured in the field. Results are shown exemplarily for one low and one high wind speed in Figure 7. RFOIL is run both with and without 3D correction model, which is one of the points of distinction from Drela's XFOIL code.

For lower wind speeds, there is a very good agreement between the 3D-corrected simulation and the field measurements. Deviations are largely found on the suction side towards the trailing edge, where RFOIL predicts separation from around 80% chord. In the binned ten-minute averaged pressure distribution, the separation point is smeared out due to variations in the underlying, time-resolved operating conditions. The

two-dimensional RFOIL simulations exhibit less congruence with the measurements.

For higher wind speeds, the use of RFOIL's 3D correction model is disadvantageous, leading to a significant overprediction of the suction peak and an underprediction of the flow separation. Contrarily, the two-dimensional simulation shows good agreement in terms of the separation point location. It can be observed that there is a discrepancy between measured and simulated stagnation pressure, preventing a better agreement between field measurements and 2D simulation for this wind speed. This stagnation pressure offset was found to increase with increasing wind speed. It is hypothesised that this is related to changes in the reference pressure, for example, due to deformations of the long reference tubing when the blade pitch angle increases.

The airfoil level comparison further corroborates findings from the blade level, namely that 3D corrections improve the match with simulations only until a certain wind speed, after which the use of such correction models yields lower agreement with the field experiment. This aligns with findings by Montgomerie et al. and Chaviaropoulos and Hansen, who link the decrease of three-dimensional flow effects with increasing wind speed to an increase in blade pitch angle [63, 67]. On the blade level, it was observed that the congruence between simulations and experiment reduces from $U_\infty = 9$ m/s. Referring back to the experimentally derived lift polar presented in Figure 4, this is also the wind speed around which the airfoil stalls in the field. This suggests that the use of 3D correction models for airfoil polars should be linked to whether or not flow separation occurs.

Remaining deviations between simulation and field might be attributed to the presence of roughness. The RFOIL simulations were run in clean conditions, whereas the surface roughness of the blade in the field is difficult to assess. While simulations with actively tripped boundary layer clearly worsened the agreement of results, the inclusion of minor levels of roughness could potentially improve the comparison. Investigating this further is, however, considered outside of this article's scope.
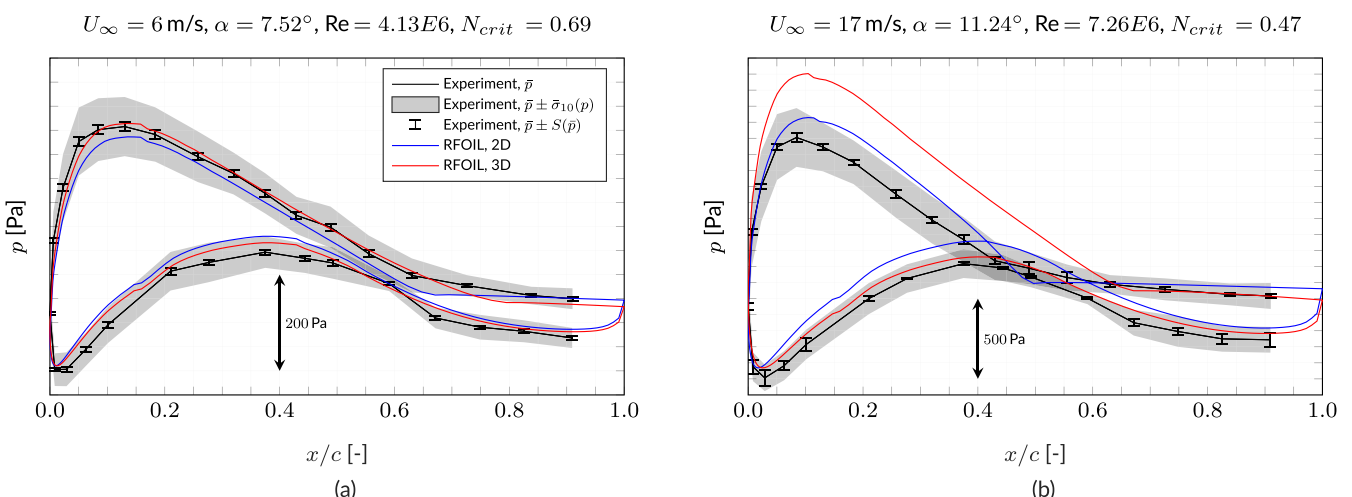

FIGURE 7 | Pressure distribution measured in the field compared to RFOIL simulation results for a low (a) and high (b) wind speed.

3.3 | Model Validation Based on Long-Term Time-Resolved Experimental Data

Next to the analysis based on ten-minute average data, an attempt is made to validate the numerical simulation model on a time-resolved scale. As described in Section 2.2.4, average operating and environmental conditions of two-minute time series are used as input to aeroelastic simulations. The simulation results are then compared to time-resolved field measurements in terms of normal and tangential force, and angle of attack. The majority of the two-minute samples have an average wind speed below or around rated conditions. Results from the previous section indicate that 3D flow corrections should be applied for these lower wind speeds. Therefore, the angle of attack estimation for the two-minute time series is done by pattern-matching the pressure measurements against RFOIL simulations with 3D correction.

Figure 8 shows the relative deviation of the simulated quantities from their measured/estimated counterpart as a function of both environmental and operational parameters. The relative deviation values are calculated for each of the approximately 1300 two-minute time series as the mean deviation between simulated and experimental values of 36 ten-degree azimuthal bins

$$E(\xi) = \frac{1}{36} \sum_{i=1}^{36} \left| \frac{\xi_{i,sim} - \xi_{i,exp,bin}}{\xi_{i,exp,bin}} \right| \qquad (25)$$

where ξ is an arbitrary variable. The modulus is calculated to avoid the cancellation of errors.

Three data points are marked separately in colour. These correspond to the cases with the lowest (green), average (blue) and highest (red) sum of deviations between simulation and experiment regarding normal and tangential force, and angle of attack, weighted by their individual mean over the approximately 1300 two-minute time series:

$$E_{sum} = \frac{E(F_n)}{\bar{E}(F_n)} + \frac{E(F_t)}{\bar{E}(F_t)} + \frac{E(\alpha)}{\bar{E}(\alpha)} \qquad (26)$$

Overall, there appears to be very little correlation between operating and environmental conditions and the error between simulation and experiment. The highest errors are found where the highest data counts are available, indicating a certain random appearance of such outliers with a growing number of data points. The only observable correlation exists for the turbulence intensity. Since the simulations use steady wind conditions, the better congruence at low turbulence intensity is not surprising. It was further investigated whether the accuracy with which the wind shear profile was approximated affected the deviations between simulation and experimental results. While no clear correlation could be observed, it should be noted that fitting a shear profile to the met mast measurements can be a source of error for all regarded time series. It is expected that the congruence of simulations and field experiment can be improved by using either the average measured wind profile or even the time-resolved wind profile data (ideally measured upstream of the turbine using, for example, a forward-facing nacelle-based LiDAR) as input to the simulations.
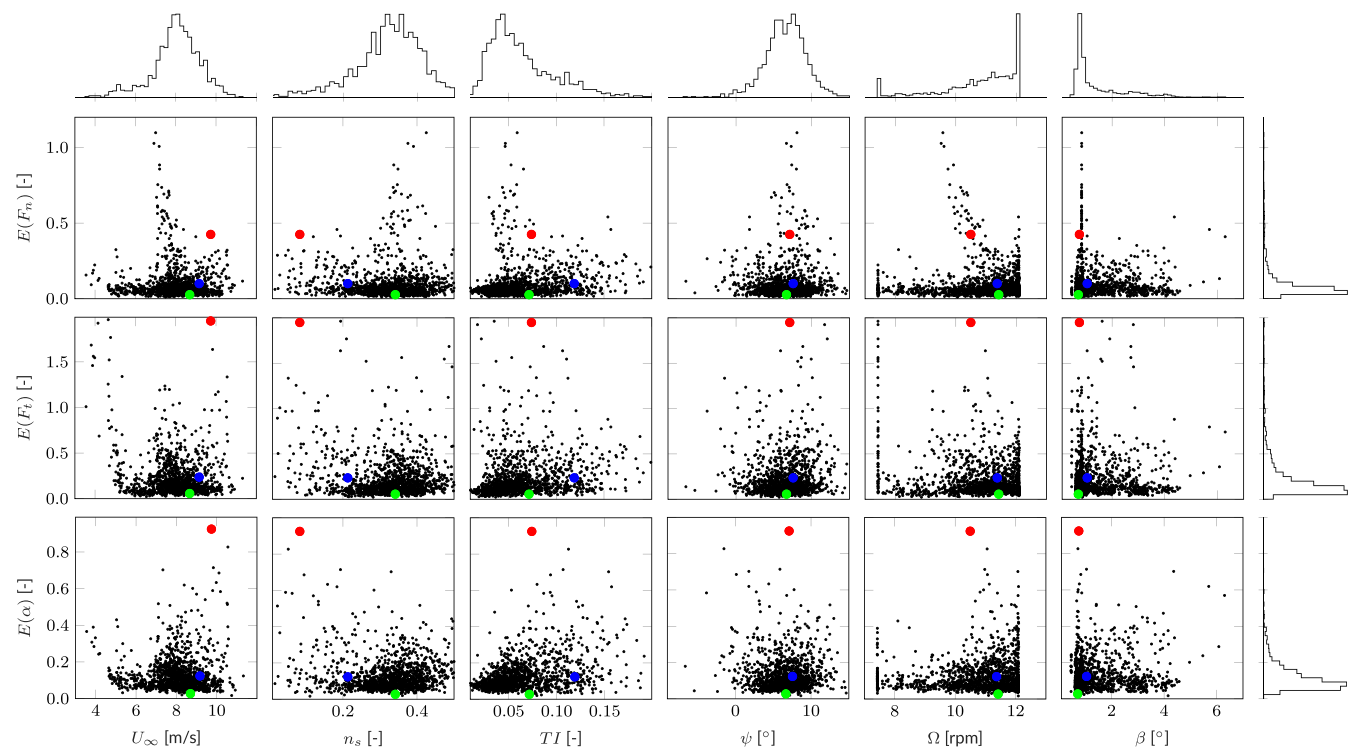

FIGURE 8 | Relative deviation of the simulated normal force, tangential force and angle of attack from their measured/estimated counterpart as a function of environmental and operational parameters; The green •, blue • and red • mark correspond to the time series with lowest, average and highest deviation between field data and simulation results, respectively.

Positively, the error distributions peak at relatively low values and quickly decay towards higher errors. The mean overall deviation between simulated and measured normal force is 10% and for the tangential force 22%. The higher value of the tangential force error can be explained by the fact that the simulations are based on viscous polars while the viscous drag, which largely contributes to the tangential force, cannot be measured using pressure taps. The mean overall relative deviation between the
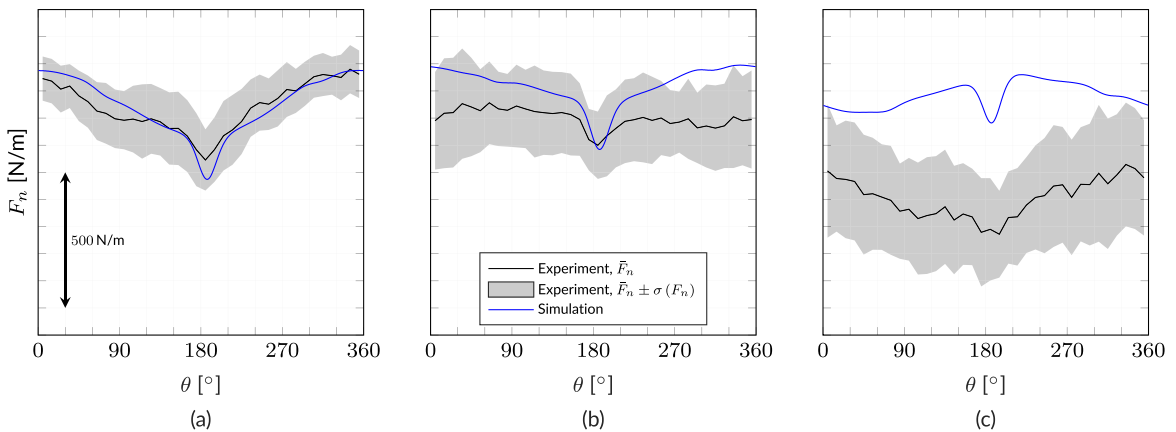

FIGURE 9 | Measured and simulated normal force as a function of azimuth for the time series with lowest (a), average (b) and highest (c) deviation between field data and simulation results (see • • • in Figure 8); subfigures with identical ordinates.
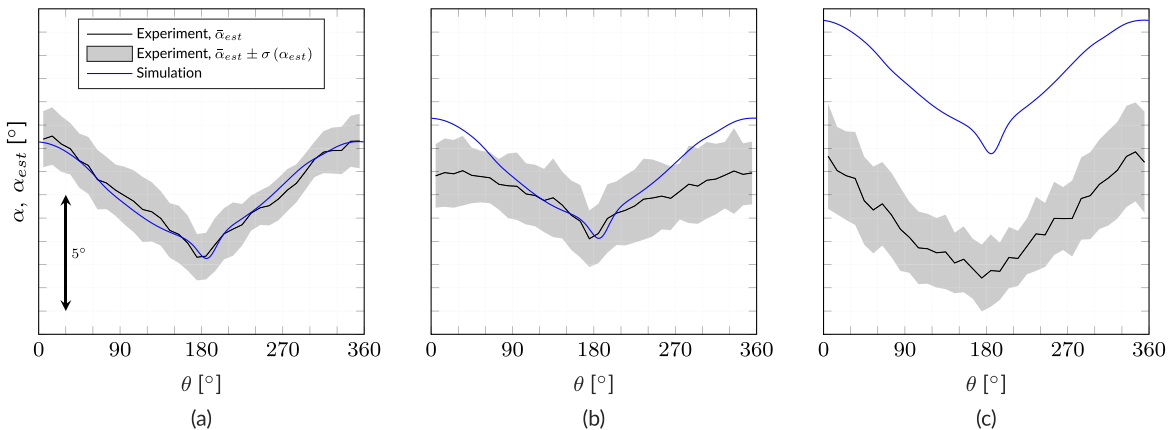
FIGURE 10 | Estimated and simulated angle of attack as a function of azimuth for the time series with lowest (a), average (b) and highest (c) deviation between field data and simulation results (see • • • in Figure 8), α refers to the simulated angle of attack while α_{est} refers to the values estimated based on the field pressure data; subfigures with identical ordinates.
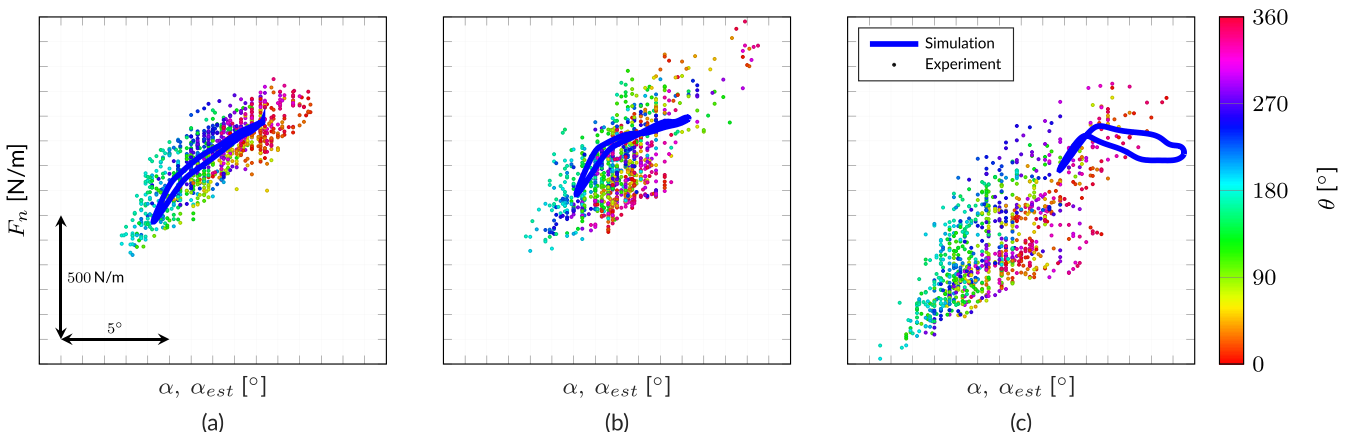
FIGURE 11 | Measured/simulated normal force as a function of the estimated/simulated angle of attack for the time series with lowest (a), average (b) and highest (c) deviation between field data and simulation results (see • • • in Figure 8), α refers to the simulated angle of attack while α_{est} refers to the values estimated based on the field pressure data; subfigures with identical abscissae and ordinates.

simulated and estimated angle of attack is 13%, which corresponds to a mean absolute deviation of 0.97°.

To illustrate in more detail what the aforementioned cases with lowest (•), average (•) and highest (•) deviation between simulation and experimental data look like, the normal force and angle of attack values are plotted as function of azimuth in Figures 9 and 10. Both simulated and experimental data clearly show the dip in axial force due to the tower passage. Figures 9a and 10a demonstrate that in the lowest deviation case, near-perfect agreement between averaged field data and simulation can be achieved. While for the average deviation case (Figures 9b and 10b), the general shape and magnitude of force and angle of attack values are still approximated reasonably well, this is not the case anymore for the highest deviation case (Figures 9c and 10c). Independent of the regarded case, the variations in the time-resolved field data cannot be captured by the steady aeroelastic simulations.

Finally, the unsteady normal force to angle of attack curves are investigated. Figure 11 shows the experimental data coloured by the azimuthal position together with the numerical results. As visible in Figure 11a, the experimental data exhibits a hysteresis, which the simulation replicates accurately. In Figure 11b,c, this hysteresis is decreasingly detectable as the experimental data scatters more randomly. Consequently, the numerical tool's ability to accurately simulate reality decreases.

4 | Conclusions

This article presents measurements obtained on a 3.8-MW field research wind turbine located in the north of the Netherlands. Pressure measurements were logged continuously over multiple months. Simultaneously, a ground-based LiDAR system provided detailed wind speed measurements across the entire turbine height.

In this study, these measurements are used for the validation of numerical models aiming at simulating reality as closely as possible. As part of this validation exercise relies on ten-minute averaged pressure distributions, it is first investigated how representative such averaged measurements are of the underlying unsteady aerodynamics. It can be shown, that only for post-stall angles of attack, generally occurring for rather high wind speeds, the ten-minute average data loses its fidelity to the time-resolved aerodynamics.

Following this analysis, the ten-minute statistics are binned by wind speed and turbulence intensity. The bin average values are used as input to BEM-based aeroelastic simulations. The simulated normal and tangential force coefficients are compared to the values determined from the measured pressure distributions. Furthermore, the simulated angle of attack and Reynolds number are used as input for RFOIL simulations, which generate pressure distributions that can directly be compared against measurements. The best match is found when clean airfoil polars are used in the aeroelastic simulations. Furthermore, it is demonstrated that the use of 3D flow correction models largely influences the agreement between simulations and field measurements. For low wind speeds, employing such a correction leads to higher congruence, while for higher wind speeds, simulations match the field measurements better without 3D flow correction. Combined with the experimental lift polar derived from the field measurements, these findings suggest that 3D flow correction models should be switched on and off as a function of the amount of flow separation occurring.

This study closes by comparing measurements and aeroelastic simulations on a time-resolved scale. On average, the measured and simulated normal force deviate by 10%. A 13% average deviation is found between the simulated angle of attack and the one estimated from the measured pressure data. The simulations' accuracy seems generally unaffected by most operating and environmental conditions, but better agreement is found for low turbulence, which more closely resembles the steady nature of the aeroelastic simulations. Depending on the individual time series, large differences between simulation and field measurements are found regarding the unsteady normal force over angle of attack curves in terms of their mean force and angle of attack level as well as the curves' shape.

In conclusion, an extensive validation campaign has been performed based on multiple months of field measurements. Results confirm that BEM-based aeroelastic tools and 2D viscous-inviscid coupled panel methods like RFOIL are still viable for the simulation of modern multi-megawatt wind turbines when provided with accurate input. Furthermore, this study corroborates the value of pressure measurements on field turbines, both regarding the analysis of blade and airfoil aerodynamics and for the validation of numerical models on these scales.

Nomenclature

Latin Letters

a, a'	Axial and tangential induction factor
c	Chord
D	Drag force
E	Relative deviation
F_n, F_t	Chord normal and tangential force
g	Gravitational constant
L	Lift force
N	Number of samples per bin
$\vec{n}$	Normal vector
n_s	Shear exponent
p	Pressure
R	Blade tip radius
Re	Reynolds number
r	Radial coordinate
S	Standard error of bin averaged mean
TI	Turbulence intensity
t	Time
U_∞	Free stream velocity
V	Velocity
V_n, V_t	Velocity normal and tangential to rotor plane
V_{rel}	Relative inflow velocity
x	Chordwise coordinate
z	Height above ground

Greek letters

α	Angle of attack
β	Blade pitch angle
ζ	Cone angle
θ	Azimuthal angle
λ	Tip-speed ratio
ξ	Arbitrary variable
ρ	Density of air
σ	Standard deviation of the bin data samples
τ	Tilt angle
ϕ	Inflow angle
ψ	Yaw angle
Ω	Rotational speed
ω	Angular velocity

Subscripts

$2D$	Two-dimensional
$3D$	Three-dimensional
10	Related to ten-minute average data
bin	Bin
$cent$	Centrifugal
cor	Corrected
dyn	Dynamic
est	Estimated
hor	Horizontal
hub	Hub
inv	Inviscid
PS	Pressure sensor
$rated$	Rated conditions
ref	Reference
sum	Sum
TS	Related to time-resolved data

Data Availability Statement

Due to commercial interests of the industrial project partners, the research data cannot be shared.

Peer Review

The peer review history for this article is available at https://www.webofscience.com/api/gateway/wos/peer-review/10.1002/we.2952.

References

1. G. J. H. van Groenewoud, L. M. M. Boermans, and J. L. van Ingen, "Investigation of Laminar-Turbulent Transition of the Boundary Layer on the 25 m HAT Wind Turbine," Report LR-390. Faculty of Aerospace Engineering, TU Delft, (1983).

2. C. P. Butterfield, W. P. Musial, and D. A. Simms, "Combined Experiment Phase 1," NREL/TP-257-4655. Office of Scientific and Technical Information (OSTI), (1992).

3. D. A. Simms, M. M. Hand, L. J. Fingersh, and D. W. Jager, "Unsteady Aerodynamics Experiment Phases II–IV Test Configurations and Available Data Campaigns," NREL/TP-500-25950. Office of Scientific and Technical Information (OSTI), (1999).

4. H. A. Madsen, "Aerodynamics of a Horizontal-Axis Wind Turbine in Natural Conditions," Risø-M-2903. Risø, (1991).

5. H. A. Madsen, "Structural Dynamics of a 100 kW HAWT," Risø-M-2887. Risø, (1991).

6. A. Bruining, "Aerodynamic Characteristics of a 10m Diameter Rotating Wind Turbine Blade," IW95-084R. IW95-084R, Delft, (1997).

7. T. Maeda and H. Kawabuchi, "Surface Pressure Measurement on a Rotating Blade of Field Horizontal Axis Wind Turbine In Yawed Condition," *JSME International Journal Series B* 48, no. 1 (2005): 156–163.

8. J. G. Schepers, A. J. Brand, A. Bruining, et al., Final Report of IEA Annex XVIII: Enhanced Field Rotor Aerodynamics Database. ECN-C-02-016. Energy Research Center of the Netherlands, (2002).

9. A. P. Schaffarczyk, D. Schwab, and M. Breuer, "Experimental Detection of Laminar-Turbulent Transition on a Rotating Wind Turbine Blade in the Free Atmosphere," *Wind Energy* 20, no. 2 (2016): 211–220.

10. C. Bak, H. A. Madsen, U. S. Paulsen, et al., "DAN-AERO MW: Detailed Aerodynamic Measurements on a Full Scale MW Wind Turbine," in *European Wind Energy Conference and Exhibition (EWEC)*, (2010): 20–23.

11. H. Madsen, P. Fuglsang, J. Romblad, et al., "The DAN-AERO MW Experiments," in *48th AIAA Aerospace Sciences Meeting Including the New Horizons Forum and Aerospace Exposition*, (American Institute of Aeronautics and Astronautics, 2010).

12. C. Bak, N. Troldborg, and H. A. Madsen, "DAN-AERO MW: Measured Airfoil Characteristics for a MW Rotor in Atmospheric Conditions," in *EWEA Annual Event 2011*, (European Wind Energy Association (EWEA), 2011).

13. N. Troldborg, C. Bak, N. N. Srensen, H. Aagaard Madsen, P.-E. Rthor, F. Zahle, and S. Guntur, "Experimental and Numerical Investigation of 3D Aerofoil Characteristics on a MW Wind Turbine," in *Proceedings - European Wind Energy Conference & Exhibition 2013*, (European Wind Energy Association (EWEA), 2013), http://www.ewea.org/annual2013/.

14. H. A. Madsen, N. N. Srensen, C. Bak, N. Troldborg, and G. Pirrung, "Measured Aerodynamic Forces on a Full Scale 2 MW Turbine in Comparison With EllipSys3D and HAWC2 Simulations," *Journal of Physics: Conference Series* 1037 (2018): 22011.

15. A. Ghadirian, G. C. Larsen, and N. Troldborg, "Comparing Rotor Plane Induction Determined From Full-Scale Measurements and CFD Simulations," *Wind Energy* 22, no. 1 (2018): 109–123.

16. C. Grinderslev, G. Vijayakumar, S. Ananthan, N. N. Srensen, F. Zahle, and M. A. Sprague, "Validation of Blade-Resolved Computational Fluid Dynamics for a MW-Scale Turbine Rotor in Atmospheric Flow," *Journal of Physics: Conference Series* 1618, no. 5 (2020): 52049.

17. T. Potentier, C. Braud, E. Guilmineau, A. Finez, and C. L. Bourdat, "Analysis of the DANAERO Wind Turbine Field Database to Assess the Importance of Different State-of-the-Art Blade Element Momentum (BEM) correction models," *Energy Science & Engineering* 9, no. 9 (2021): 1477–1500.

18. K. Boorsma, G. Schepers, H. Aagard Madsen, et al., "Progress in the Validation of Rotor Aerodynamic Codes Using Field Data," *Wind Energy Science* 8, no. 2 (2023): 211–230, https://wes.copernicus.org/articles/8/211/2023/.

19. H. A. Madsen, T. Barlas, A. Fischer, A. S. Olsen, and A. G. Gonzalez, "Inflow and Pressure Measurements on a Full Scale Turbine With a Pressure Belt and a Five Hole Pitot Tube," *Journal of Physics: Conference Series* 2265, no. 2 (2022): 22096. Publisher: IOP Publishing.

20. A. Gamberini, T. Barlas, A. Gomez Gonzalez, and H. A. Madsen, "Validation of Aeroelastic Dynamic Model of Active Trailing Edge Flap System Tested on a 4.3 MW Wind Turbine," *Wind Energy Science* 9, no. 5 (2024): 1229–1249, https://wes.copernicus.org/articles/9/1229/2024/.

21. P. Doubrawa, C. Kelley, and J. Naughton, "RAAW," (2023), https://www.osti.gov/servlets/purl/1984650/.

22. S. Letizia, N. Bodini, P. Brugger, A. Scholbrock, N. Hamilton, F. Portgel, P. Doubrawa, and P. Moriarty, "Holistic Scan Optimization of Nacelle-Mounted Lidars for Inflow and Wake Characterization at the RAAW and AWAKEN Field Campaigns," *Journal of Physics: Conference*

Series 2505, no. 1 (2023): 12048. https://iopscience.iop.org/article/10.1088/1742-6596/2505/1/012048.

23. A. Rybchuk, L. A. Martnez-Tossas, N. Hamilton, P. Doubrawa, G. Vijayakumar, M. Hassanaly, M. B. Kuhn, and D. S. Zalkind, "A Baseline for Ensemble-Based, Time-Resolved Inflow reconstruction for a Single Turbine Using Large-Eddy Simulations and Latent Diffusion Models," *Journal of Physics: Conference Series* 2505, no. 1 (2023): 12018. https://iopscience.iop.org/article/10.1088/1742-6596/2505/1/012018.

24. K. Brown, P. Bortolotti, E. Branlard, et al., "One-to-One Aeroservoelastic Validation of Operational Loads and Performance of a 2.8 MW Wind Turbine Model in OpenFAST," *Wind Energy Science* 9, no. 8 (2024): 1791–1810. https://doi.org/10.5194/wes-9-1791-2024.

25. M. M. Hand, D. A. Simms, L. J. Fingersh, D. W. Jager, J. R. Cotrell, S. Schreck, and S. M. Larwood, "Unsteady Aerodynamics Experiment Phase VI: Wind Tunnel Test Configurations and Available Data Campaigns," NREL/TP-500-29955. Office of Scientific and Technical Information (OSTI), (2001).

26. K. Boorsma and J. G. Schepers, "Description of Experimental Set-Up. Mexico Measurements," ECN-X-09-0XX. Energy Research Center of the Netherlands, (2009).

27. K. Boorsma and J. G. Schepers, "Rotor Experiments in Controlled Conditions Continued: New Mexico," *Journal of Physics: Conference Series* 753, no. 2 (2016): 22004. https://iopscience.iop.org/article/10.1088/1742-6596/753/2/022004.

28. J. G. Schepers and S. J. Schreck, "Aerodynamic Measurements on Wind Turbines," *Wiley Interdisciplinary Reviews: Energy and Environment* 8, no. 1 (2018): e320.

29. P. J. Eecen, S. A. M. Barhorst, H. Braam, et al., "Measurements at the ECN Wind Turbine Test Station Wieringermeer," RX-06-055. Energy Research Center of the Netherlands, (2006).

30. L. A. H. Machielse, "Validatiemetingen EWTW, eindrapport," ECN-E-06-062. Energy Research Center of the Netherlands, (2006).

31. PDOK, "Map of EWEF Test Site, Derived From Data Provided by PDOK (Publieke Dienstverlening op de Kaart), Licensed Under the CC-BY-4.0 License, Accessed on 20/03/2024," (2024), https://app.pdok.nl/viewer.

32. E. K. Fritz, C. L. Kelley, and K. A. Brown, "On Optimizing the Sensor Spacing for Pressure Measurements on Wind Turbine Airfoils," *Wind Energy Science* 9, no. 8 (2024): 1713–1726. https://doi.org/10.5194/wes-9-1713-2024.

33. C. Lindenburg, "PHATAS User's Manual Version 11737," WMC-2016-005. LM Wind Power (Confidential), (2020).

34. C. Lindenburg, "PHATAS Release "NOV-2003" and "APR-2005" User's Manual," WMC-2016-005. Energy Research Centre of the Netherlands, (2005).

35. K. Boorsma, F. Grasso, and J. Holierhoek, "Enhanced Approach for Simulation of Rotor Aerodynamic Loads," in *Proceedings of EWEA Offshore*, (2011), https://publications.tno.nl/publication/34631408/75n2Es/m12003.pdf.

36. H. Snel, "Heuristic Modelling of Dynamic Stall Characteristics," in *EWEC-CONFERENCE-*, (Bookshop for Scientific Publications, 1997): 429–433.

37. R. P. J. O. M. Van Rooij, "Modification of the Boundary Layer Calculation in RFOIL for Improved Airfoil Stall Prediction," IW-96087R, (Netherlands, 1996).

38. M. Drela, *XFOIL: An Analysis and Design System for Low Reynolds Number airfoils*, Lecture Notes in Engineering (Springer Berlin Heidelberg, 1989): 1–12.

39. G. Ramanujam, H. Özdemir, and H. W. M. Hoeijmakers, "Improving Airfoil Drag Prediction," *Journal of Aircraft* 53, no. 6 (2016): 1844–1852, https://doi.org/10.2514/1.C033788.

40. M. O. L. Hansen and J. Johansen, "Tip Studies Using CFD and Comparison With Tip Loss Models," *Wind Energy* 7, no. 4 (2004): 343–356.

41. J. Johansen and N. N. Sørensen, "Aerofoil Characteristics From 3D CFD Rotor Computations," *Wind Energy* 7, no. 4 (2004): 283–294.

42. H. Rahimi, M. Hartvelt, J. Peinke, and J. G. Schepers, "Investigation of the Current Yaw Engineering Models for Simulation of Wind Turbines in BEM and Comparison With CFD and Experiment," *Journal of Physics: Conference Series* 753 (2016): 22016.

43. I. Herrez, E. Daniele, and J. G. Schepers, "Extraction of the Wake Induction and Angle of Attack on Rotating Wind Turbine Blades From PIV and CFD Results," *Wind Energy Science* 3, no. 1 (2018): 1–9.

44. W. Z. Shen, M. O. L. Hansen, and J. N. Sørensen, "Determination of Angle Of Attack (AOA) for Rotating Blades," *Wind energy* (Berlin Heidelberg: Springer, 2007): 205–209.

45. W. Z. Shen, M. O. L. Hansen, and J. N. Sørensen, "Determination of the Angle of Attack on Rotor Blades," *Wind Energy* 12, no. 1 (2009): 91–98.

46. E. Jost, L. Klein, H. Leipprand, T. Lutz, and E. Krmer, "Extracting the Angle of Attack on Rotor Blades From CFD Simulations," *Wind Energy* 21, no. 10 (2018): 807–822.

47. W. Zhong, W. Z. Shen, T. G. Wang, and W. J. Zhu, "A New Method of Determination of the Angle of Attack on Rotating Wind Turbine Blades," *Energies* 12, no. 20 (2019): 4012.

48. H. Rahimi, J. G. Schepers, W. Z. Shen, N. R. García, M. S. Schneider, D. Micallef, C. J. S. Ferreira, E. Jost, L. Klein, and I. Herrez, "Evaluation of Different Methods for Determining the Angle of Attack on Wind Turbine Blades With CFD Results Under Axial Inflow Conditions," *Renewable Energy* 125 (2018): 866–876.

49. K. Vimalakanthan, J. G. Schepers, W. Z. Shen, H. Rahimi, D. Micallef, C. J. S. Ferreira, E. Jost, and L. Klein, "Evaluation of Different Methods of Determining the Angle of Attack on Wind Turbine Blades Under Yawed Inflow Conditions," *Journal of Physics: Conference Series* 1037 (2018): 22028.

50. S. Guntur and N. N. Sørensen, "An Evaluation of Several Methods of Determining the Local Angle of Attack on Wind Turbine Blades," *Journal of Physics: Conference Series* 555 (2014): 12045.

51. A. Bruining, G. J. W. Van Bussel, G. P. Corten, and W. A. Timmer, "Pressure Distribution From A Wind Turbine Blade; Field Measurements Compared To 2-Dimensional Wind Tunnel Data," Institute for Windenergy, Delft University of Technology (1993).

52. H. Snel, R. Houwink, and T. Bosscher, "Sectional Prediction of Lift Coefficients on Rotating Wind Turbine Blades in Stall," ECN-C-93-052. Energy Research Center of the Netherlands, (1994).

53. D. J. Laino, A. C. Hansen, and J. E. Minnema, "Validation of the AeroDyn Subroutines Using NREL Unsteady Aerodynamics Experiment Data," *Wind Energy* 5, no. 2-3 (2002): 227–244.

54. C. Bak, J. Johansen, and P. B. Andersen, "Three-Dimensional Corrections of Airfoil Characteristics Based on Pressure Distributions," in *Proceedings of the European Wind Energy Conference*, (2006): 1–10.

55. J. L. Tangler, "The Nebulous Art of Using Wind-Tunnel Airfoil Data for Predicting Rotor Performance," in *ASME 2002 Wind Energy Symposium*, (2002).

56. J. L. Tangler, "Insight Into Wind Turbine Stall and Post-Stall Aerodynamics," *Wind Energy* 7, no. 3 (2004): 247–260.

57. T. Sant, G. van Kuik, and G. J. W. van Bussel, "Estimating the Angle of Attack From Blade Pressure Measurements on the NREL Phase VI Rotor Using a Free Wake Vortex Model: Axial Conditions," *Wind Energy* 9, no. 6 (2006): 549–577.

58. T. Sant, G. van Kuik, and G. J. W. van Bussel, "Estimating the Angle of Attack From Blade Pressure Measurements on the National

Renewable Energy Laboratory Phase VI Rotor Using a Free Wake Vortex Model: Yawed Conditions," *Wind Energy* 12, no. 1 (2009): 1–32.

59. D. Micallef, M. Kloosterman, C. Ferreira, T. Sant, and G. van Bussel, "Validating BEM, Direct and Inverse Free Wake Models With the MEXICO Experiment," in *48th AIAA Aerospace Sciences Meeting Including the New Horizons Forum and Aerospace Exposition*, (American Institute of Aeronautics and Astronautics, 2010).

60. A. Bruining and W. A. Timmer, "Airfoil Characteristics of Rotating Wind Turbine Blades," *Journal of Wind Engineering and Industrial Aerodynamics* 39, no. 1-3 (1992): 35–39.

61. D. E. Shipley, M. S. Miller, M. C. Robinson, M. W. Luttges, and D. A. Simms, "Techniques for the Determination of Local Dynamic Pressure and Angle of Attack on a Horizontal Axis Wind Turbine," NREL/TP-442-7393. Office of Scientific and Technical Information (OSTI), (1995).

62. A. Saini and A. Gopalarathnam, "Leading-Edge Flow Sensing for Aerodynamic Parameter Estimation," *AIAA Journal* 56, no. 12 (2018): 4706–4718.

63. B. O. G. Montgomerie, A. J. Brand, J. Bosschers, and R. P. J. O. M. Van Rooij, "Three-Dimensional Effects in Stall," ECN-C-96-079. Energy Research Center of the Netherlands, (1996).

64. L. M. Mack, "Transition and Laminar Instability," JPL-PUBL-77-15, (1977), https://ntrs.nasa.gov/citations/19770017114.

65. M. Drela and H. Youngren, *A User's Guide to MISES 2.53* (Cambridge, MA: Massachusetts Institute of Technology, 1998).

66. T. Coelho Leite Fava, B. A. Lobo, A. Schaffarczyk, M. Breuer, D. S. Henningson, and A. Hanifi, "Numerical Investigation of Transition on a Wind Turbine Blade Under Free-Stream Turbulence at Rec = 1,000,000," (2023), https://urn.kb.se/resolve?urn=urn:nbn:se:kth:diva-337112, preprint.

67. P. K. Chaviaropoulos and M. O. L. Hansen, "Investigating Three-Dimensional and Rotational Effects on Wind Turbine Blades by Means of a Quasi-3D Navier-Stokes Solver," *Journal of Fluids Engineering* 122, no. 2 (2000): 330–336, https://asmedigitalcollection.asme.org/fluidsengineering/article/122/2/330/459646/Investigating-ThreeDimensional-and-Rotational.